

**Observation of near E_F Fermi-arc van Hove singularity
with prominent coupling to phonon in a van der Waals coupled Weyl semimetal**

Z. Wang*^{1,2}, Cheng-Yi Huang*³, Chia-Hsiu Hsu*^{4,5,6}, Hiromasa Namiki⁷, Tay-Rong Chang⁸,
Feng-Chuan Chuang^{5,6}, H. Lin³, Takao Sasagawa⁷, Vidya Madhavan², and Yoshinori Okada⁴

¹*Department of Physics, University of Science and Technology of China, Hefei, Anhui 230026, China.*

²*Department of Physics and*

Frederick Seitz Materials Research Laboratory,

University of Illinois Urbana-Champaign, Urbana, IL 61801, USA

³*Institute of Physics, Academia Sinica, Taipei, Taiwan*

⁴*Quantum Materials Science Unit, Okinawa Institute of Science and Technology (OIST),*

Okinawa 904-0495, Japan

⁵*Department of Physics, National Sun Yat-sen University, Kaohsiung 80424, Taiwan*

⁶*Physics Division, the National Center for Theoretical Sciences, Hsinchu 30013, Taiwan*

⁷*Laboratory for Materials and Structures, Tokyo Institute of Technology,*

4259 Nagatsuda, Midori-ku, Yokohama, Kanagawa 226-8503, Japan

⁸*National Cheng Kung University, Taiwan*

A van der Waals (vdW) coupled Weyl semimetal material NbIrTe₄ is investigated by combining scanning tunneling microscopy/spectroscopy (STM/S) and first-principles calculations. We observe a sharp peak in the tunneling conductance near the zero bias energy, and its origin is ascribed to a van Hove singularity (vHs) associated with a Lifshitz transition of the topologically none trivial Fermi arc states. Furthermore, tunneling spectroscopy measurements show a surprisingly large signature of electron–boson coupling, which presumably represents anomalously enhanced electron–phonon coupling through the enhanced charge susceptibility. Our finding in vdW coupled material is particularly invaluable due to applicable exfoliation technology for searching exotic topological states by further modulating near E_F vHs in nano-flake and its nano-device.

Introduction

The band structure near the Fermi energy (E_F) governs the physical properties of fermionic systems. A particularly interesting situation arises when there is a sharp peak in the density of states (DOS) near the E_F [1,2,3,4,5,6,7,8,9,10,11,12,13,14]. One of the most exotic cases is that of high-temperature superconductor cuprates, in which the parent state is a half-filled two-dimensional (2D) square lattice [14]. Based on a simple tight binding without consider strong interactions, a van Hove singularity (vHs) exists near the E_F , and its important role of vHs for superconductivity has been suggested [14]. In general, whenever a band-structure-related sharp peak in the DOS coincides with the E_F , such as a vHs, it is intrinsically susceptible to Fermi surface instabilities, which can be a substantial driving force for various emergent phases, including unconventional superconductivity, density wave state, and magnetism, with the added possibility of multiple coexisting phases [14]. Dimensionality plays a critical role in Fermi surface instability because the band nesting condition and electron interaction are inherently enhanced by transitioning from three dimensions (3D) to 2D (and one dimension (1D)). Furthermore, the enhancement of electron–boson coupling, associated with enlarged susceptibility and Fermi surface instability, often becomes important [14,15]. Such phenomenology with band anomalies near the E_F has been observed and extensively discussed for several material classes, such as van der Waals Dirac materials [5,6], Fe-based high- T_c superconductors [7], magnetic Kagome systems [8,9,10], and strongly correlated oxides [11,12,13]. In particular, importance of van der Waals (vdW) coupled materials hosting near E_F vHs has been growing due to applicable advanced exfoliation technology to further tailor vHs, as in graphene [5].

An interesting area in this field is the investigation of many-body effects in topological edge states. For example, prior experiments on topological crystalline insulators have revealed the vHs associated with a Lifshitz transition of the surface state [16]. However, the associated DOS peaks are far from the E_F [17,18,19]. Other promising topological materials include the Weyl semimetals. Weyl semimetals feature pairs of doubly degenerate Weyl cones with a linear dispersion around the Weyl nodes in the bulk and Fermi arcs on the surface [20,21,22,23]. An important feature is that the surface Fermi arc states eventually morph into bulk-like states, that is, sinking into a pair of Weyl points with opposite charge chirality. Recent studies on the band structure of Weyl semimetals have suggested a possible topological Lifshitz transition near the Weyl points with an interesting surface Fermi arc that rewires at different energies [24,25,26]. However, a singularity with a peak in the DOS near the E_F has not been directly investigated experimentally.

In this study, we combine scanning tunneling microscopy/spectroscopy (STM/S) and first-principles calculations to investigate a vdW coupled Weyl semimetal, NbIrTe_4 . This ternary compound has attracted considerable interest as a type-II semimetal possessing relatively simple topological Fermi arc states with fewer Weyl points than those of MoTe_2 [27,28,29,30,31]. Using STM/S, we report the discovery of a near- E_F vHs associated with a Lifshitz transition of the topological Fermi arc states in NbIrTe_4 . Additionally, STS shows surprisingly prominent electron–boson coupling features, which could be a consequence of the sharp DOS peak from the topological vHs near the E_F .

Results and Discussions

Crystal structure and topographic image

The crystal structure of NbIrTe₄ from side and top views are shown in Figure 1a and b, respectively. The expected crystalline structure is 1T, and the termination is (001) surface with the van-der-Waals-coupled Te atomic sheet. A topographic image of NbIrTe₄ is shown in Figure 1c, and its inset shows zoomed-in image. Figure 1d shows the topographic height evolution along lines in the inset of Figure 1c. Compared with 1T-MoTe₂, it is expected that the lattice periodicity along the *b*-axis is larger in NbIrTe₄ owing to the alternate ordering of Nb and Ir rows (Figure 1b). The periodicity along *a* (green arrow) and *b* (purple arrow) directions are about 12.6 Å and 3.8 Å, respectively. Indeed, these values are consistent with the expected crystal structure of NbIrTe₄ (see arrows in Figure 1b and d).

Conductance peak near zero bias voltage

The most remarkable experimental observation in this study is sharp *dI/dV* peak close to the zero bias voltage energy $eV_B=0$. Here, zero bias voltage corresponds to experimental E_F position. To demonstrate this striking observation, we show a spatial evolution of line cut of the *dI/dV* along a line trace of approximately 350 nm (Figure 1c) and its spatially averaged spectra (Figure 1f). Importantly, the sharp *dI/dV* peak is homogeneously distributed on the surface. Thus, near zero bias energy *dI/dV* peak is not due to the disorder-originated local state. In addition, we confirmed that observation of near $eV_B=0$ *dI/dV* peak was reproducible by using different fresh tips, while the peak position was not always pinned at $eV_B=0$ but its position differ within 10 meV scale depending on area by area separated by long distant (supplemental note 1 for details). As we introduce later, theoretical three energies for Weyl point (WP), to be compared with experiment, are indicated in Figure 1f. Also, near $eV_B=0$ spectral anomaly reflecting electron-boson coupling are indicated by arrows, as we discuss later.

Experimental Quasi particle interference (QPI)

We performed quasiparticle interference (QPI) measurements to reveal the momentum origin of the experimental near E_F DOS peak. QPI has been widely used to investigate the topological surface states in Weyl semimetals [32,33,34,35,36,37]. The *dI/dV* map at $eV_B=+110$ meV shows faint real-space scattering patterns confined sharply near the scattering centers, which represent quasiparticle states with short lifetimes (Figure 2a and its inset). On the other hand, the *dI/dV* map at $eV_B = +10$ meV shows apparent wave-like patterns that can be tracked over several wavelengths (Figure 2b and its inset). Characteristic standing wave vectors can be visualized in the *q* space from the energy evolution of the Fourier transform (FT) of the *dI/dV* maps (Figure 2c-f). Figure 2g shows energy evolution of QPI channel along q_x , which is along *a*-axis in the real space and the Γ -Y direction in the momentum space (Figure 3a). As seen, dispersion is clearly observed in wide energy range (from $eV_B \sim 0$ up to 300 meV). An important feature to emphasize here is dramatic change of sharpness in QPI pattern between near $eV_B=0$ and high energy. While QPI channel is blunt at high energy (Figure 2c), near $eV_B=0$ QPI pattern shows multiple well-

defined channels $q_1 \sim q_3$ in FT image (Figure 2e). This trend in FT image is consistent with standing wave pattern in real space (inset of Figure 2 and Figure 2a-b). We note that NbIrTe_4 hosts much sharper interference pattern around $eV_B=0$, compared to the QPI observation in $(\text{Mo,W})\text{Te}_2$ [33,34,35,36,37,38]. Hereafter, we present theoretical band structure in this system, followed by its comparison with experimental QPI dispersion.

Density functional theory (DFT)

To understand the band structure and topological nature of NbIrTe_4 , we conducted density functional theory (DFT) calculation. Figure 3a shows Brillouin zone (BZ) of bulk (lower) and surface (upper). The three pairs of irreducible Weyl points (WP1, WP2, and WP3) are found in DFT calculation (see also supplemental note 2 for details). The pairs of Weyl points are reflected by mirror symmetry or glide symmetry (time-reversal symmetry) with opposite (equivalent) chiral charges. As shown in Figure 3b, irreducible WPs are depicted by color-coded circles and squares in the first BZ with their energies E_{WP1} , E_{WP2} , and E_{WP3} (136 meV, 134 meV, and -86 meV, respectively). Figure 3c and d show the total-surface-spectral-weight maps at 134 and -50 meV, respectively. Here, it is known that the spectral weight of the topologically nontrivial Fermi arc surface state (NSS) sinks into the bulk state through Weyl points. Thus, by looking for this characteristic spectral fingerprint, NSS can be qualitatively disentangled with trivial surface state (TSS). The momentum region highlighted by the pink rectangle in Figure 3c clearly represents that spectra indicated by arrow (NSS2) sinks into the bulk bands through WP2, as shown in Figure 3e. Similarly, tracking spectral sinking into WP3 enable us to assign another Fermi arc portion. Figure 3f shows dispersion along the vertical line with an arrow in Figure 3d, and spectral feature indicated by arrow (NSS3) sinks into the bulk bands through WP3. Here, the spectral weight sinking behavior into WP2 and WP3 in the momentum space are highlighted by the dashed curve in Figure 3e and f, respectively.

We briefly point theoretical observation of unusual connection of NSS2 and NSS3 in momentum space and their characteristic atomic nature. Figure 3g shows energy evolution of total surface spectral weight (NSS and TSS) along k_x at fixed $k_y=\pi/b$ (see horizontal arrows in Figure 3c). Around the momentum highlighted by dashed circle, NSS2 and NSS3 merge with each other. This means that NSS2 and NSS3 host a single Fermi arc state, which connect two pairs of Weyl points (a total of four Weyl points) instead of the conventional case where only one pair of Weyl points is connected. This behavior is topologically allowed since number of nontrivial surface states emerging from each Weyl node with chiral charge-1 remains one. While we leave understanding details for future theoretical study, we think it is possible that this connection is not accidental. Another, feature we find from band calculation is dominant contribution of Nb atom for constructing NSS (see also supplemental note 3 for details). Figure 3h is atomic character dependence of spectral weight dispersion shown in Figure 3g. Dominant contribution of Nb atom for NSS2 and NSS3 are clearly visualized (see arrows). In this report, we simply identify the NSS from TSS, based on the relative spectral weight of Nb than that of Ir/Te. The ambiguity of threshold does not have an issue within the main purpose of this study.

Calculated surface spectral weight shows existence of a Lifshitz transition of nontrivial Fermi arcs at characteristic energy. We define this characteristic energy as E_{vHs} , whose theoretical value is around -60 meV in pristine DFT calculation (see vertical axis of Figure 3g and h). By focusing on the momentum region highlighted by rectangle in Figure 3d, the detailed energy evolution of the Fermi arcs within a small energy interval near the E_{vHs} are shown in Figure 4a-e. The interaction and eventual merging of the two bands result in a saddle point in the dispersion, that is, the formation of a vHs. As highlighted by the dashed circle in Figure 4c, we observe a geometrical change in the constant energy contour shape at E_{vHs} , which is the Lifshitz transition happening at this energy. The calculated DOS of the NSS exhibits an apparent peak at the corresponding energy E_{vHs} (Figure 4f). To further check momentum origin of this peak, we plot the calculated dispersion of the NSS (upper panel in Figure 4g) by zooming in around the momentum of band touching, together with a map of $1/|\nabla_k E|$ in the momentum space (lower panel in Figure 4g). As the total DOS is proportional to $\int 1/|\nabla_k E(k)| dk$, the $1/|\nabla_k E|$ map provides an excellent way to visualize the characteristic momentum leading to an enhanced DOS. As shown in Figure 3g, an apparent correspondence can be observed between the Lifshitz transition (upper panel) and the large DOS (lower panel). A next important step is matching energy between theory and experiment to address the momentum origin of the experimental DOS peak near E_F . Adjusting energy between theory and experiment is ordinary required process due to miss estimation of E_F in DFT calculation and/or inherent chemical doping/displacement in NbIrTe₄ phase. While clarifying microscopic origin is beyond the scope of this study, natural expectation for possible chemical origin is Te vacancy and/or displacement between Ir and Nb.

Comparison between experiment and theory

Based on agreement between experimental QPI and theoretical joint density of state (JDOS) patterns, we conclude that experimental near E_F DOS peak originates from vHs of NSS. We first show comparison between experimental QPI (Figure 5a) and JDOS from both NSS and TSS (Figure 5b). Note that energy axis of theoretical JDOS is set as $E-E_{\text{vHs}}$. Clear agreement seen in this comparison strongly supports that experimental $eV_B = 0$ roughly corresponds to theoretical E_{vHs} . Furthermore, theoretical spectral weight distribution of TSS and NSS near E_{vHs} and experimental E_F are beautifully captured by experimental QPI pattern. To demonstrate this, theoretical spectral weight distribution in k_x - k_y plane for $E-E_{\text{vHs}}=10$ meV, as well as scattering vector candidates (q_{TSS} , q_{NSS1} , q_{NSS2} , and q_{NSS3}) is shown first (Figure 5c). Focusing on 10 meV other than E_F is simply due to higher experimental signal to noise, which brings much cleared comparison, and the momentum area highlighted by rectangle in Figure 5c is where we focus in Figure 4 to demonstrate vHs associated with Lifshitz transition. By comparing QPI patterns at $eV_B = 10$ meV (Figure 5d upper) and theoretical JDOS solely from NSS at $E-E_{\text{vHs}}=10$ meV (Figure 5d lower), experimental three characteristic channels q_1 , q_2 , q_3 , and their extension in q_x - q_y space are beautifully explained as intra-scattering channel q_{NSS1} , q_{NSS2} , and q_{NSS3} , respectively. Since JDOS simply captures QPI, we expect spin-

based matrix element is not totally diagonal for $q_{\text{nss}1}$, $q_{\text{nss}2}$, and $q_{\text{nss}3}$. Furthermore, absence of q_{tss} means our QPI data are dominated by the NSS near the E_F . Note that TSS contains either Te or Ir components while NSS is dominated Nb component. Thus, for understanding missing experimental q_{tss} , we think the orbital related matrix element in scattering processing play a dominant role instead of the selection of spin-based matrix element effect. Based on comparison between theory and experiment mentioned here, we conclude that experimental dI/dV originates from vHs associated with the Lifshitz transition of NSS.

Experimental electron-boson coupling

Interestingly, prominent spectroscopic signature of electron boson coupling appears in experimental dI/dV near E_F . Existence of prominent electron boson coupling is along with the fact that slight quantitative mismatch between experimental scattering vectors and theoretical JDOS without considering interaction (see Figure 5). Figure 6a shows a topographic image in which 2116 tunneling spectra were acquired near the E_F . The averaged spectra are shown in (Figure 6b). Peak-dip features, which are symmetric with respect to the E_F , are observed in the tunneling spectrum (dI/dV) and its derivative (d^2I/dV^2), indicating a strong coupling of electrons to a bosonic mode. Here, we define E_p as the DOS peak energy and E^+ and E^- as the peak positions in d^2I/dV^2 . The area in Figure 6a and Figure 1-2 are different, and this presumably lead slight difference of E_p in Figure 1f and Figure 6b (see also supplemental note 1 for details).

We observe periodic modulations in the intensity of the DOS peak and features related to the electron–mode coupling. To present this variation, we simply show the spatial evolution of the topographic height (Figure 6d), dI/dV (Figure 6e), and d^2I/dV^2 (Figure 6f) across lines A-B in Figure 5a. It can be observed that both the peak intensity at the E_p and the features at E^+ and E^- vary in real space with the crystal lattice. These spatial variations of peak intensity at E_p with lattice periodicity can be naturally understood, as our DFT calculation indicates that the dominant contribution in the formation of the vHs of the NSS is from Nb (Figure 3h and supplementary note 3). Importantly, E^+ and E^- appear almost symmetrically relative to the E_F at every location, which further supports that these features at E^+ and E^- are related to the electron–mode coupling. As our system is not magnetic, the bosonic mode is more likely to be a phonon. Indeed, the energy scale of $|E^+|$ and $|E^-|$ is comparable to that of the calculated phonon energy while our current comparison is with bulk phonon, leaving direct comparison with surface phonon for future study (supplemental note 5 for details). Note that we observed no evidence of gap opening and an additional order on the surface of NbIrTe_4 despite the presence of a significant peak in the DOS near the E_F . This is rather intriguing, given that strong electron–boson coupling can be revealed from the STM data.

A spectroscopic observation of prominent electron–phonon coupling with a topological vHs is not trivial. For example, in the case of Z_2 topological insulators, electron–phonon coupling is not observed to have a large signal [39,40,41,42]. In contrast, a recent transport study of a Weyl semimetal, WP_2 , has reported dominant electron–phonon interactions [43]. While the nature of the surface has not been clarified, our observations suggest an intriguing interplay between the topological vHs formation and enhanced

electron–phonon coupling. Notably, our experimentally observed DOS peak is much sharper than that obtained from a noninteracting model (Figure 4f), which encourages microscopic theoretical studies for a detailed understanding of the many-body effects in topological Fermi arc states in Weyl semimetals. Furthermore, our findings provide an interesting route to modulate the Fermi arc states via phonon engineering [44,45,46,47,48]. While phonon is a reasonable origin, as discussed possible other bosonic mode coupling is not totally excluded. For example, acoustic plasmon mode is reported recently in Bi_2Te_3 [49], and possible multiple nature of bosonic mode coupling may further enrich many-body effects on near E_F topological vHs.

Summary

In summary, we report the discovery of formation of a DOS peak near the E_F on the surface of the Weyl semimetal NbIrTe_4 . Combined with the experimental observation of sharp QPI patterns and theoretical calculations, we find the origin of the experimental near- E_F DOS peak is the formation of a vHs associated with the Lifshitz transition in topologically none-trivial Fermi arc states. Our observation indicates the intriguing interplay between the formation of the near- E_F topological vHs and enhanced electron–phonon coupling, which paves the way for the manipulation of topologically nontrivial states in Weyl semimetals via phonon engineering. Our finding in vdW coupled material is particularly invaluable due to applicable exfoliation technology for searching exotic topological states by further modulating near E_F vHs in nano-flake and its nano-device.

Methods

Crystal growth and STM experiments

The single crystals NbIrTe_4 were grown by a Te-flux method. The samples were characterized by XRD and XRF to confirm single phase without phase segregation. Samples were cleaved in ultra-high vacuum at about 80 K and then immediately inserted into the cold STM head. All the data were obtained around 300 mK in zero external magnetic field. Different W and PtIr tips were used and checked on Cu(111) surface. The tunneling conductance (dI/dV), which is proportional to DOS, were measured using standard lock-in technique with voltage modulation at 987.5 Hz.

The density functional theory (DFT) band calculation

The density functional theory (DFT) band calculation was performed using the projector augmented wave method as implemented in the VASP package [50] within the generalized gradient approximation (GGA) [51]. In all of calculation, the spin-orbit coupling (SOC) was included self-consistently.

Acknowledgements

Work at the University of Illinois, Urbana-Champaign was supported by U.S. Department of Energy (DOE), Office of Science, Office of Basic Energy Sciences (BES), Materials Sciences and Engineering Division under Award # DE-SC0022101. Z.Y.W. is supported by National Natural Science Foundation of China (No. 12074364) and the Fundamental Research Funds for the Central Universities (WK3510000012). This work was, in part, supported by a JST-CREST project [JPMJCR16F2] and a JSPS Grants-in-Aid for Scientific Research (A) [21H04652].

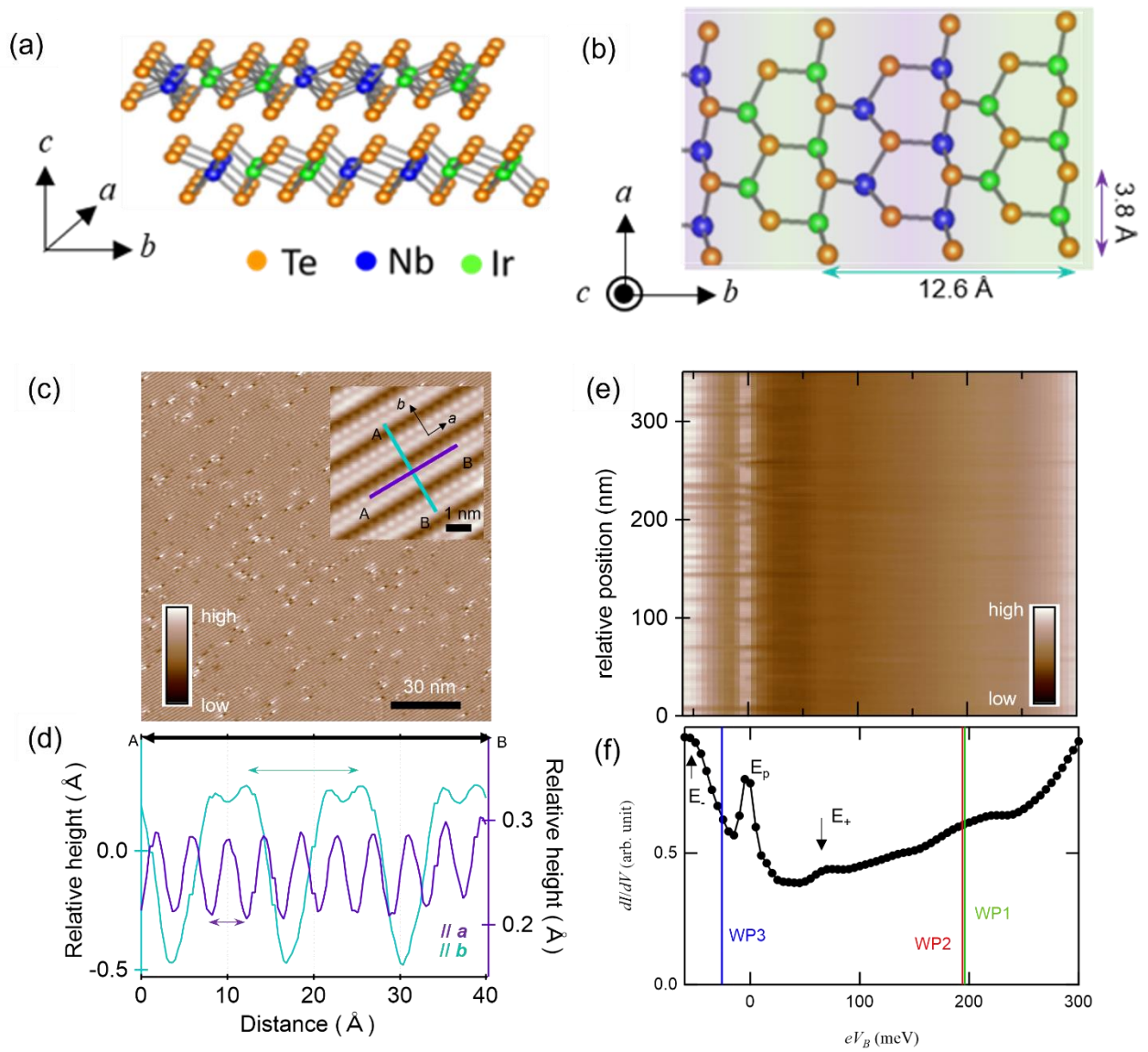


Figure 1. Characteristics of the Weyl semimetal NbIrTe₄.

(a-b) Schematic of the crystal structure of NbIrTe₄ with side and top views, respectively. **(c)** STM topographic image (I_t=100 pA and V_B=100 mV). **(d)** Topographic height variations along two lines in the inset of (c). **(e)** Homogeneous spatial evolution of dI/dV spectra along a 350 nm line on the surface, and **(f)** the spatial average of dI/dV curve.

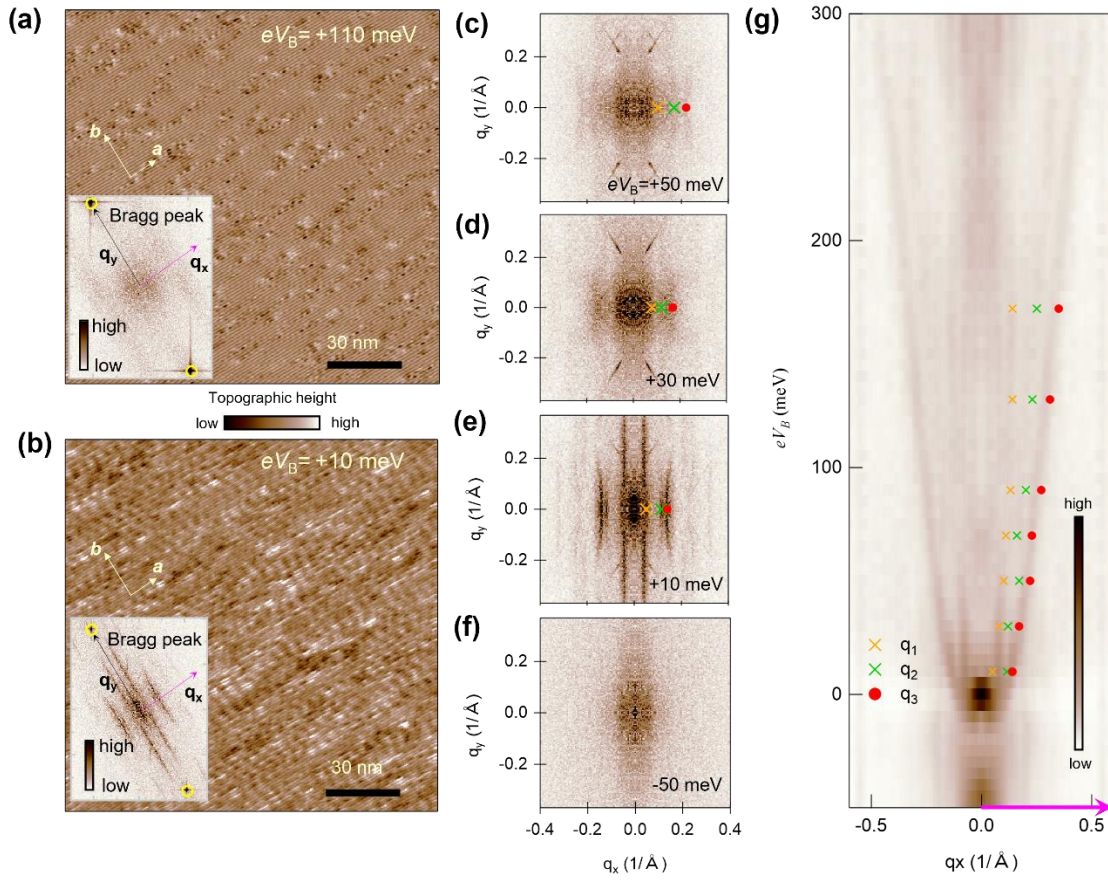


Figure 2. QPI patterns of NbIrTe₄ surface.

(a-b) Conductance (dI/dV) maps at $eV_B = 110$ and 10 meV, respectively. The insets show the raw Fourier transformation (FT) of the dI/dV images, where Bragg peaks are highlighted by circles. (c-f) Energy evolution of FT of dI/dV maps, which are zoomed in around $q=0$ to emphasize the interference patterns. Here, the horizontal and vertical axes are set along the crystal axes a and b , respectively. Also, these images are rotated and two-fold symmetrized. (g) Intensity plot of the line cut in the FTs along the q_x direction at $q_y=0$, together with scattering vectors.

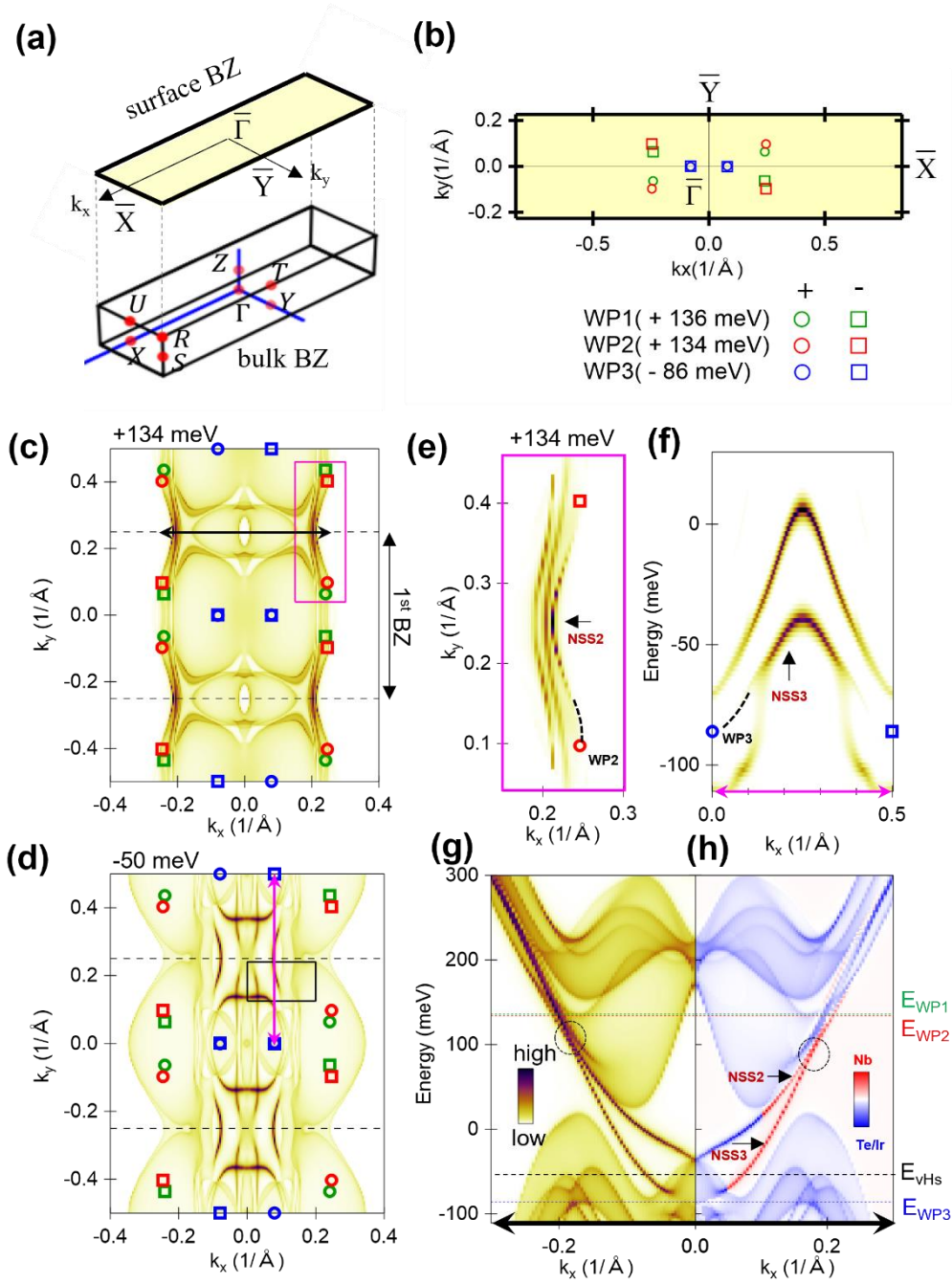


Figure 3. The Density functional theory (DFT) calculation for electronic state of NbIrTe4.

(a) BZ of the system. (b) The calculated WPs with their momentum, energy, and chirality. (c-d) Total spectral weight on the surface plotted at 134 meV, the energy of WP2, and near the Fermi energy at -50 meV. The total surface spectral weight contains TSS and NSS contributions. The Weyl points WP1 (green), WP2 (red), and WP3 (blue) are indicated in the momentum space. (e) Zoomed-in image of the pink rectangle in (c), and (f) dispersion along the pink line in (d). The dashed lines indicate the trace along which the NSSs sink into the bulk state through Weyl points in (e) and (f). (g) Energy dispersion along the k_x direction at $k_y = \pi/b$ [see horizontal line in (c)] for total spectral weight and (h) its atomic character dependence.

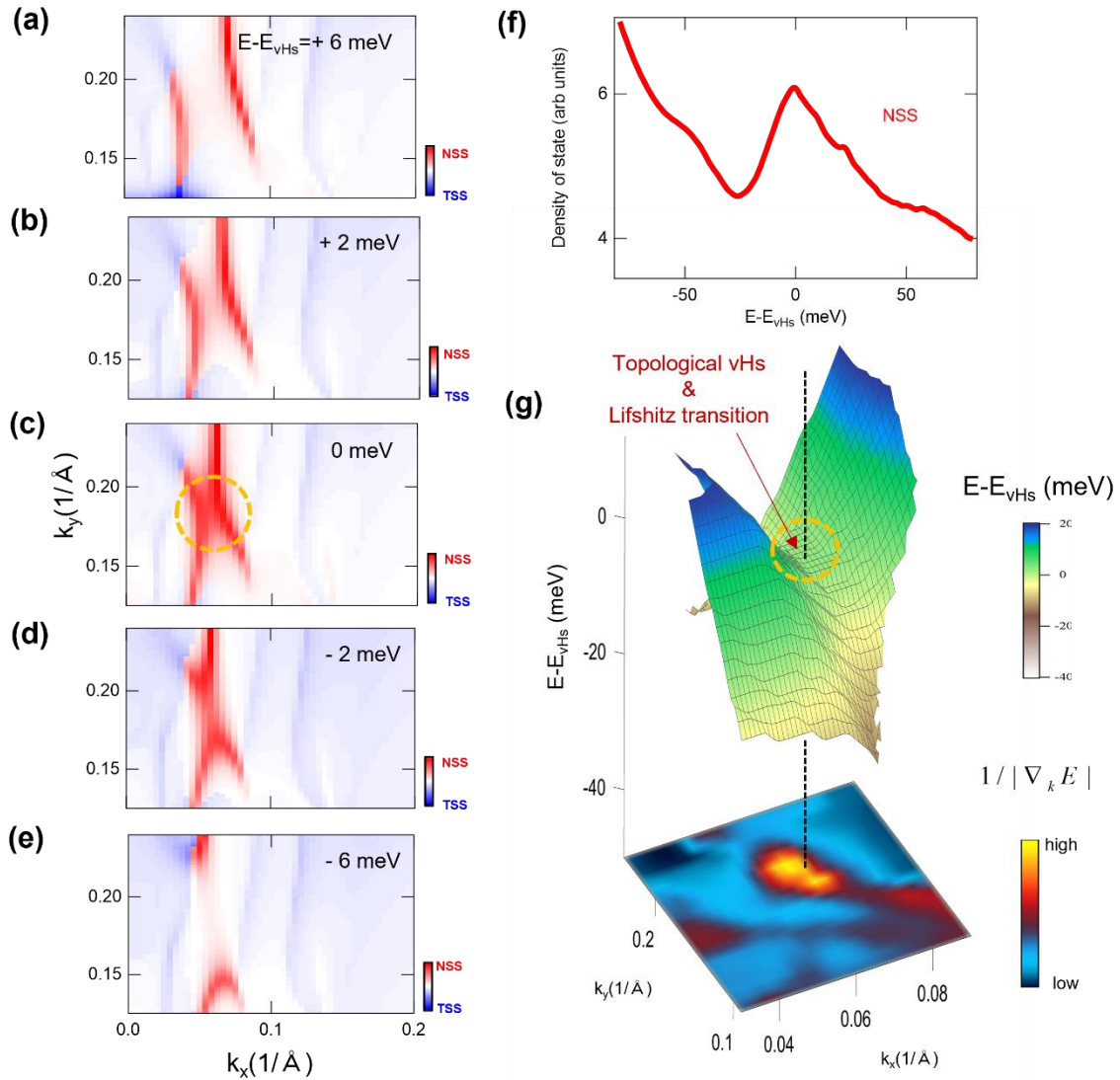


Figure 4. Electronic structure calculation near the energy for van hove singularity E_{vHs} .

(a-e) Energy evolution of spectral weight for the area indicated by the dashed rectangle in **Fig. 3(d)**. **(f)** Calculated DOS for NSS, which is obtained by integrating the spectral weight over all the momenta in the first BZ. **(g)** 3D display of NSS dispersion (upper part) and $1/|\nabla_k E|$ (lower part), near the critical momentum (dashed circle in (c)). The vHs formations associated with a Lifshitz transition are indicated by an arrow and dashed circle in (c) and (g).

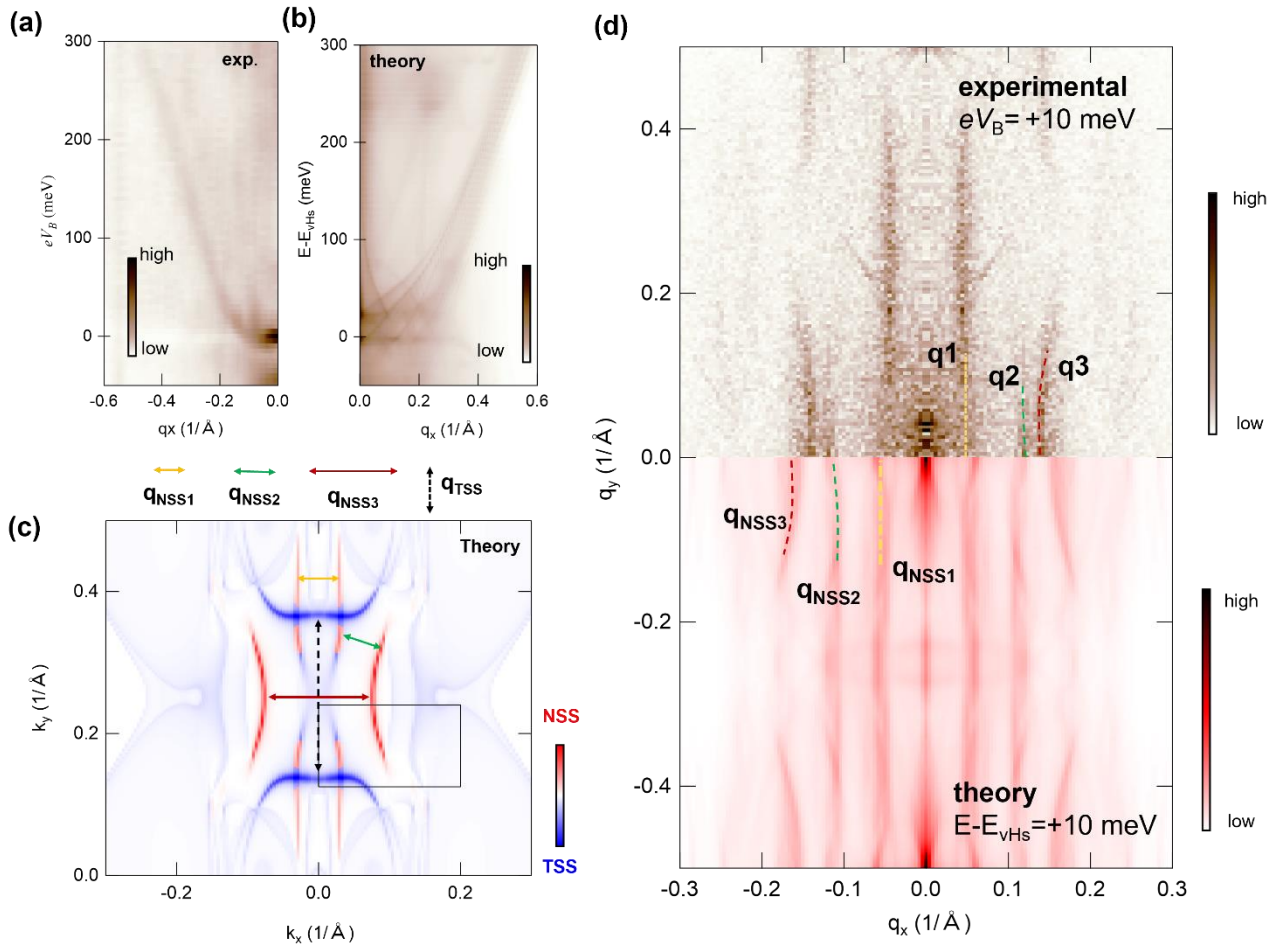


Figure 5. The comparison between theory and experiments

(a) The experimental energy evolution of QPI pattern along q_x direction. (b) The theoretical autocorrelation of the total spectral weight (JDOS) along the q_x direction at $q_y=0$. Here, vertical axis is plotted energy relative to vHs, which is $E-E_{vHs}$. (c) Calculated spectral weight at $E-E_{vHs} = 10$ meV. Here, the rectangle is the momentum area focused in detail in Fig. 4. (d) Comparison between the experimental interference pattern (upper) and calculation based on NSS (lower) at $eV_B = 10$ meV and $E-E_{vHs} = 10$ meV, respectively.

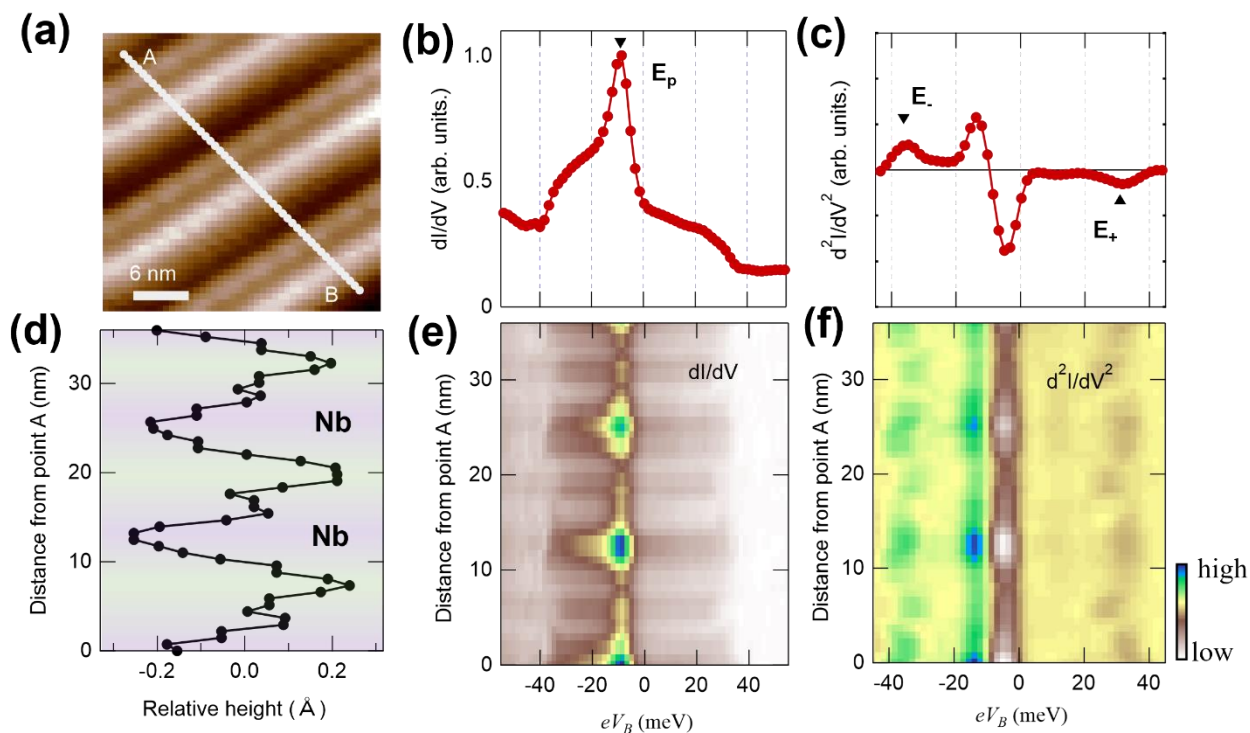


Figure 6. Enhanced electron–mode coupling.

(a) Topographic image ($I_t=100$ pA and $V_B=100$ mV). (b–c) Spatial average of dI/dV and d^2I/dV^2 spectra. The spectra are averaged from 2116 curves (46×46 pixels) from the area shown in (a). (d) Topographic height variations along A-B in (a). (e–f) Spatial evolution of dI/dV and d^2I/dV^2 spectra taken along A-B shown in (a).

References

- ¹ Van Hove, L. The Occurrence of Singularities in the Elastic Frequency Distribution of a Crystal. *Phys. Rev.* **89**, 1189 (1953)
- ² Madhavan, V.; Chen, W.; Jamneala, T.; Crommie, M. F.; Wingreen, N. S. Tunneling into a single magnetic atom: spectroscopic evidence of the Kondo resonance. *Science* **280**, 567–569 (1998)
- ³ Schmidt, A. R.; Hamidian, M. H.; Wahl, P.; Meier, F.; Balatsky, A. V.; Garrett, J. D.; Williams, T. J.; Luke, G. M.; Davis, J. C. Imaging the Fano lattice to ‘hidden order’ transition in URu₂Si₂. *Nature* **465**, 570–576 (2010)
- ⁴ Aynajian, P.; Neto, E. H. S.; Gyenis, A.; Baumbach, R. E.; Thompson, J. D.; Fisk, Z.; Bauer, E. D.; Yazdani, A. Visualizing heavy fermions emerging in a quantum critical Kondo lattice. *Nature* **486**, 201–206 (2012)
- ⁵ Li, G.; Luican, A.; Lopes dos Santos, J. M. B.; Castro Neto, A. H.; Reina, A.; Kong, J.; Andrei, E. Y. Observation of Van Hove singularities in twisted graphene layers. *Nat. Phys.* **6**, 109 (2010)
- ⁶ Chichinadze, D. V.; Classen, L.; Chubukov, A. V. Valley magnetism, nematicity, and density wave orders in twisted bilayer graphene. *Phys. Rev. B* **102**, 125120 (2020)
- ⁷ Shi, X.; Han, Z.-Q.; Peng, X.-L.; Richard, P.; Qian, T.; Wu, X.-X.; Qiu, M.-W.; Wang, S. C.; Hu, J. P.; Sun, Y.-J.; Ding, H. Enhanced superconductivity accompanying a Lifshitz transition in electron-doped FeSe monolayer. *Nat. Commun.* **8**, 14988 (2017)
- ⁸ Zhang, S. S.; Yin, J.-X.; Ikhlas, M.; Tien, H.-J.; Wang, R.; Shumiya, N.; Chang, G.; Tsirkin, S. S.; Shi, Y.; Yi, C.; Guguchia, Z.; Li, H.; Wang, W.; Chang, T.-R.; Wang, Z.; Yang, Y.-f.; Neupert, T.; Nakatsuji, S.; Hasan, M. Z. Many-Body Resonance in a Correlated Topological Kagome Antiferromagnet. *Phys. Rev. Lett.* **125**, 046401 (2020)
- ⁹ Lin, Z.; Choi, J. H.; Zhang, Q.; Qin, W.; Yi, S.; Wang, P.; Li, L.; Wang, Y.; Zhang, H.; Sun, Z.; Wei, L.; Zhang, S.; Guo, T.; Lu, Q.; Cho, J. H.; Zeng, C.; Zhang, Z. Flat bands and Emergent Ferromagnetic Ordering in Fe₃Sn₂ Kagome Lattices. *Phys. Rev. Lett.* **121**, 096401 (2018)
- ¹⁰ Yin, J.-X.; Shumiya, N.; Mardanya, S.; Wang, Q.; Zhang, S. S.; Tien, H.-J.; Multer, D.; Jiang, Y.; Cheng, G.; Yao, N.; Wu, S.; Wu, D.; Deng, L.; Ye, Z.; He, R.; Chang, G.; Liu, Z.; Jiang, K.; Wang, Z.; Neupert, T.; Agarwal, A.; Chang, T.-R.; Chu, C.-W.; Lei, H.; Hasan, M. Z. Fermion–boson many-body interplay in a frustrated kagome paramagnet. *Nat. Commun.* **11**, 4003 (2020)
- ¹¹ Iwaya, K.; Satow, S.; Hanaguri, T.; Shannon, N.; Yoshida, Y.; Ikeda, S. I.; He, J. P.; Kaneko, Y.; Tokura, Y.; Yamada, T.; Takagi, H. Local Tunneling Spectroscopy across a Metamagnetic Critical Point in the Bilayer Ruthenate Sr₃Ru₂O₇. *Phys. Rev. Lett.* **99**, 05720 (2007)
- ¹² Wang, Z.; Walkup, D.; Derry, P.; Scaffidi, T.; Rak, M.; Vig, S.; Kogar, A.; Zeljkovic, I.; Husain, A.; Santos, L. H.; Wang, Y.; Damascelli, A.; Maeno, Y.; Abbamonte, P.; Fradkin, E.; Madhavan, V. Quasiparticle interference and strong electron–mode coupling in the quasi-one-dimensional bands of Sr₂RuO₄. *Nat. Phys.* **13**, 799–805 (2017)

- ¹³ Marques, C. A.; Rhodes, L. C.; Fittipaldi, R.; Granata, V.; Yim, C. M.; Buzio, R.; Gerbi, A.; Vecchione, A.; Rost, A. W.; Wahl, P. The surface layer of Sr₂RuO₄: A two-dimensional model system for magnetic-field-tuned quantum criticality. arXiv:2005.00071 (2020)
- ¹⁴ Markiewicz, R. S. A survey of the Van Hove scenario for high-T_c superconductivity with special emphasis on pseudogaps and striped phases. *J. Phys. Chem. Solids* **58**, 1179–1310 (1997)
- ¹⁵ Burganov, B.; Adamo, C.; Mulder, A.; Uchida, M.; King, P. D. C.; Harter, J. W.; Shai, D. E.; Gibbs, A. S.; Mackenzie, A. P.; Uecker, R.; Bruetzsch, M.; Beasley, M. R.; Fennie, C. J.; Schlom, D. G.; Shen, K. M. Strain Control of Fermiology and Many-Body Interactions in Two-Dimensional Ruthenates. *Phys. Review Lett.* **116**, 197003 (2016)
- ¹⁶ Hsieh, T. H.; Lin, H.; Liu, J.; Duan, W.; Bansil, A.; Fu, L. Topological crystalline insulators in the SnTe material class. *Nat. Commun.* **3**, 982 (2012)
- ¹⁷ Okada, Y.; Serbyn, M.; Lin, H.; Walkup, D.; Zhou, W.; Dhital, C.; Neupane, M.; Xu, S.; Wang, Y. J.; Sankar, R.; Chou, F.; Bansil, A.; Hasan, M. Z.; Wilson, S. D.; Fu, L.; Madhavan, V. Observation of Dirac node formation and mass acquisition in a topological crystalline insulator. *Science* **341**, 1496–1499 (2013)
- ¹⁸ Zeljkovic, I.; Okada, Y.; Serbyn, M.; Sankar, R.; Walkup, D.; Zhou, W.; Liu, J.; Chang, G.; Wang, Y. J.; Hasan, M. Z.; Chou, F.; Lin, H.; Bansil, A.; Fu, L.; Madhavan, V. Dirac mass generation from crystal symmetry breaking on the surfaces of topological crystalline insulators. *Nat. Mater.* **14**, 318–324 (2015)
- ¹⁹ Zeljkovic, I.; Scipioni, K. L.; Walkup, D.; Okada, Y.; Zhou, W.; Sankar, R.; Chang, G.; Wang, Y. J.; Lin, H.; Bansil, A.; Chou, F. C.; Wang, Z.; Madhavan, V. Nanoscale determination of the mass enhancement factor in the lightly doped bulk insulator lead selenide. *Nat. Commun.* **4**, 6659 (2015)
- ²⁰ Murakami, S. Phase transition between the quantum spin Hall and insulator phases in 3D: emergence of a topological gapless phase. *New J. Phys.* **9**, 356 (2007)
- ²¹ Wan, X.; Turner, A. M.; Vishwanath, A.; and Savrasov, S. Y. Topological semimetal and Fermi-arc surface states in the electronic structure of pyrochlore iridates. *Phys. Rev. B* **83**, 205101 (2011)
- ²² Burkov, A. A.; Balents, L. Weyl Semimetal in a Topological Insulator Multilayer. *Phys. Rev. Lett.* **107**, 127205 (2011)
- ²³ Xu, G.; Weng, H.; Wang, Z.; Dai, X.; Fang, Z. Chern Semimetal and the Quantized Anomalous Hall Effect in HgCr₂Se₄. *Phys. Rev. Lett.* **107**, 186806 (2011)
- ²⁴ Volovik, G. E. Topological Lifshitz transitions. *Low Temp. Phys.* **43**, 57–67 (2017)
- ²⁵ Yang, H. F.; Yang, L. X.; Liu, Z. K.; Sun, Y.; Chen, C.; Peng, H.; Schmidt, M.; Prabhakaran, D.; Bernevig, B. A.; Felser, C.; Yan, B. H.; Chen, Y. L. Topological Lifshitz transitions and Fermi arc manipulation in Weyl semimetal NbAs. *Nat. Commun.* **10**, 3478 (2019)
- ²⁶ Ekahana, S. A.; Li, Y. W.; Sun, Y.; Namiki, H.; Yang, H. F.; Jiang, J.; Yang, L. X.; Shi, W. J.; Zhang, C. F.; Pei, D.; Chen, C.; Sasagawa, T.; Felser, C.; Yan, B. H.; Liu, Z. K.; Chen, Y. L. Topological Lifshitz transition of the intersurface Fermi-arc loop in NbIrTe₄. *Phys. Rev. B* **102**, 085126 (2020)
- ²⁷ Kumar, D.; Hsu, C.-H.; Sharma, R.; Chang, T.-R.; Yu, P.; Wang, J.; Eda, G.; Liang, G.; Yang, H., *Room-temperature nonlinear Hall effect and wireless radiofrequency rectification in Weyl semimetal TaIrTe₄* *Nat. Nanotechnol.* online (2021); arXiv: 2012.14104 (2020)

- ²⁸ Koepnick, K.; Kasinathan, D.; Efremov, D. V.; Khim, S.; Borisenko, S.; Büchner, B.; van den Brink, J. TaIrTe₄: A ternary type-II Weyl semimetal. *Phys. Rev. B* **93**, 201101(R) (2016)
- ²⁹ Li, L.; Xie, H.-H.; Zhao, J.-S.; Liu, X.-X.; Deng, J.-B.; Hu, X.-R. Ternary Weyl semimetal NbIrTe₄ proposed from first-principles calculation. *Phys. Rev. B* **96**, 024106 (2017)
- ³⁰ Belopolski, I.; Yu, P.; Sanchez, D. S.; Ishida, Y.; Chang, T. R.; Zhang, S. S.; Xu, S. Y.; Zheng, H.; Chang, G.; Bian, Jeng, H. T.; Kondo, T.; Lin, H.; Liu, Z.; Shin, S.; Hasan, M. Z. Signatures of a time-reversal symmetric Weyl semimetal with only four Weyl points. *Nat. Commun.* **8**, 942 (2017)
- ³¹ Zhou, X.; Liu, Q.; Wu, Q.; Nummy, T.; Li, H.; Griffith, J.; Parham, S.; Waugh, J.; Emmanouilidou, E.; Shen, B.; Yazyev, O. V.; Ni, N.; Dessau, D. Coexistence of tunable Weyl points and topological nodal lines in ternary transition-metal telluride TaIrTe₄. *Phys. Rev. B* **97**, 241102(R) (2018)
- ³² Inoue, H.; Gyenis, A.; Wang, Z.; Li, J.; Oh, S. W.; Jiang, S.; Ni, N.; Bernevig, B. A.; Yazdani, A. Quasiparticle interference of the Fermi arcs and surface-bulk connectivity of a Weyl semimetal. *Science* **351**, 6278 (2016)
- ³³ Zheng, H.; Bian, G.; Chang, G.; Lu, H.; Xu, S. Y.; Wang, G.; Chang, T. R.; Zhang, S.; Belopolski, I.; Alidoust, N.; Sanchez, D. S.; Song, F.; Jeng, H. T.; Yao, N.; Bansil, A.; Jia, S.; Lin, H.; Hasan, M. Z. Atomic-Scale Visualization of Quasiparticle Interference on a Type-II Weyl Semimetal Surface. *Phys. Rev. Lett* **117**, 266804 (2016)
- ³⁴ Deng, P.; Xu, Z.; Deng, K.; Zhang, K.; Wu, Y.; Zhang, H.; Zhou, S.; Chen, X. Revealing Fermi arcs and Weyl nodes in MoTe₂ by quasiparticle interference mapping. *Phys. Rev. B* **95**, 245110 (2017)
- ³⁵ Lin, C. L.; Arafune, R.; Liu, R. Y.; Yoshimura, M.; Feng, B.; Kawahara, K.; Ni, Z.; Minamitani, E.; Watanabe, S.; Shi, Y.; Kawai, M.; Chiang, T. C.; Matsuda, I.; Takagi, N. Visualizing Type-II Weyl Points in Tungsten Ditelluride by Quasiparticle Interference. *ACS Nano* **11**, 11459–11465 (2017)
- ³⁶ Iaia, D.; Chang, G.; Chang, T.-R.; Hu, J.; Mao, Z.; Lin, H.; Yan, S.; Madhavan, V. Searching for topological Fermi arcs via quasiparticle interference on a type-II Weyl semimetal MoTe₂. *npj Quantum Mater.* **3**, 38 (2018)
- ³⁷ Morali, N.; Batabyal, R.; Nag, P. K.; Liu, E.; Xu, Q.; Sun, Y.; Yan, B.; Felser, C.; Avraham, N.; Beidenkopf, H. Fermi-arc diversity on surface terminations of the magnetic Weyl semimetal Co₃Sn₂S₂. *Science* **365**, 1286–1291 (2019)
- ³⁸ Wang, Z.; Olivares, J.; Namiki, H.; Pareek, V.; Dani, K.; Sasagawa, T.; Madhavan, V.; Okada, Y. Visualizing superconductivity in an inversion-symmetry- broken doped Weyl semimetal. *Physical Rev. B* (in press)
- ³⁹ Pan, Z.-H.; Fedorov, A. V.; Gardner, D.; Lee, Y. S.; Chu, S.; Valla, T. Measurement of an Exceptionally Weak Electron-Phonon Coupling on the Surface of the Topological Insulator Bi₂Se₃ Using Angle-Resolved Photoemission Spectroscopy. *Phys. Rev. Lett.* **108**, 187001 (2012)
- ⁴⁰ Zhu, X.; Santos, L.; Howard, C.; Sankar, R.; Chou, F. C.; Chamon, C.; El-Batanouny, M. Electron-Phonon Coupling on the Surface of the Topological Insulator Bi₂Se₃ Determined from Surface-Phonon Dispersion Measurements. *Phys. Rev. Lett.* **108**, 185501 (2012)
- ⁴¹ Kondo, T.; Nakashima, Y.; Ota, Y.; Ishida, Y.; Malaeb, W.; Okazaki, K.; Shin, S.; Kriener, M.; Sasaki, S.; Segawa, K.; Ando, Y., Anomalous dressing of Dirac Fermions in the topological surface state of Bi₂Se₃, Bi₂Te₃, and Cu-Doped Bi₂Se₃. *Phys. Rev. Lett.* **110**, 217601 (2013)

- ⁴² Zhu, X.; Howard, C.; Guo, J.; El-Batanouny, M. Electron-Phonon Coupling on the Surface of Topological Insulators. arXiv:1307.4559 (2013)
- ⁴³ Osterhoudt, G. B.; Wang, Y.; Garcia, C. A. C.; Plisson, V. M.; Gooth, J.; Felser, C.; Narang, P.; Burch, K. S. Evidence for Dominant Phonon–Electron Scattering in Weyl Semimetal WP_2 . *Phys. Rev. X* **11**, 011017 (2021)
- ⁴⁴ Thomsen, C.; Strait, J.; Vardeny, Z.; Maris, H. J.; Tauc, J.; Hauser, J. J. Coherent phonon generation and detection by picosecond light pulses. *Phys. Rev. Lett.* **53**, 989–992 (1984)
- ⁴⁵ He, B.; Zhang, C.; Zhu, W.; Li, Y.; Liu, S.; Zhu, X.; Wu, X.; Wang, X.; Wen, H.-h.; Xiao, M. Coherent optical phonon oscillation and possible electronic softening in WTe_2 crystals. *Sci. Rep.* **6**, 30487 (2016)
- ⁴⁶ Gustafsson, M. V.; Aref, T.; Kockum, A. F.; Ekström, M. K.; Johansson, G.; Delsing, P. Propagating phonons coupled to an artificial atom. *Science* **346**, 207 (2014)
- ⁴⁷ Yokoi, M.; Fujiwara, S.; Kawamura, T.; Arakawa, T.; Aoyama, K.; Fukuyama, H.; Kobayashi, K.; Niimi, Y. Negative resistance state in superconducting $NbSe_2$ induced by surface acoustic waves. *Sci. Adv.* **6**, eaba1377 (2020)
- ⁴⁸ Nakamura, A.; Shimojima, T.; Chiashi, Y.; Kamitani, M.; Sakai, H.; Ishiwata, S.; Li, H.; Ishizaka, K., Nanoscale Imaging of Unusual Photoacoustic Waves in Thin Flake VTe_2 . *Nano Lett.*, 2020, 20, 4932–4938
- ⁴⁹ Jia, X.; Zhang, S.; Sankar, R.; Chou, F. C.; Wang, W.; Kempa, K.; Plummer, E. W.; Zhang, J.; Zhu, X.; Guo, J. Anomalous Acoustic Plasmon Mode from Topologically Protected States. *Phys. Rev. Lett.* **119**, 136805 (2017)
- ⁵⁰ Kresse, G.; Hafner, J. Ab initio molecular dynamics for open-shell transition metals. *Phys. Rev. B* **48**, 13115 (1993)
- ⁵¹ Perdew, J. P.; Burke, K.; Ernzerhof, M. Generalized gradient approximation made simple. *Phys. Rev. Lett.* **77**, 3865 (1996)